Journal of Asian Ceramic Societies 2 (2014) 176–184

Contents lists available at ScienceDirect

Journal of Asian Ceramic Societies

journal homepage: www.elsevier.com/locate/jascer

# Synthesis and electrical conductivity of $(La_{1-x}Sr_x)(Al_{1-y}Mg_y)O_{3-\delta}$ perovskite solid solution

Yoshihiro Hirata[a,*], Akiko Shinomiya[a], Ikuno Mukai[a], Soichiro Sameshima[a], Taro Shimonosono[a], Naoki Matsunaga[b]

[a] Department of Chemistry, Biotechnology, and Chemical Engineering, Kagoshima University, 1-21-40 Korimoto, Kagoshima 890-0065, Japan
[b] Department of Environmental Robotics, University of Miyazaki, 1-1 Gakuen-Kihanadai, Miyazaki 889-2192, Japan

ARTICLE INFO

*Article history:*
Received 24 December 2013
Received in revised form 1 March 2014
Accepted 19 March 2014
Available online 13 April 2014

*Keywords:*
Electrical conductivity
Oxide ion conductivity
Sintering
Perovskite
Solid solution

ABSTRACT

Perovskite solid solution powders with $(La_{1-x}Sr_x)(Al_{1-y}Mg_y)O_{3-\delta}$ composition (shorten as LSAM) were prepared by a coprecipitation method using corresponding aqueous solutions and ammonium carbonate solution. The freeze-dried powders were heated in air at 1500 °C for 10 h, and subsequently sintered at 1400 °C for 12 h in air. The X-ray diffraction patterns and the lattice parameters for the compositions of $x = 0$–$0.4$ at $y = 0.1$ and $y = 0$–$0.15$ at $x = 0.2$ suggested the formation of rhombohedral $LaAlO_3$ solid solution. The sinterability of LSAM was controlled by the diffusion rate of A site cations and increased by increasing Sr composition at A site and by decreasing Mg composition at B site. The highest electrical conductivity was measured at the composition of $(La_{0.8}Sr_{0.2})(Al_{0.9}Mg_{0.1})O_{2.85}$ ($6.79 \times 10^{-3}$ S/cm at 600 °C, activation energy 98.8 kJ/mol). Although the sintered $(La_{0.8}Sr_{0.2})(Al_{0.9}Mg_{0.1})O_{2.85}$ electrolyte contained 28% porosity, its conductivity was higher than the conductivity of dense 8 mol% yttria-stabilized zirconia electrolyte. The conductivity and activation energy of LSAM greatly vary according to the concentration of available oxygen vacancy and the association of positively charged oxygen vacancy and negatively charged $Sr'_{La}$ sites or $Mg'_{Al}$ sites. The LSAM composition of $(La_{0.8}Sr_{0.2})(Al_{0.9}Mg_{0.1})O_{2.85}$ provided the perovskite structure of the smaller strain (tolerance factor 1.007). This is another factor for the highest conductivity.



## 1. Introduction

$(La_{1-x}Sr_x)(Ga_{1-y}Mg_y)O_{3-\delta}$ perovskite structure solid solution shows a higher oxide ion conductivity than yttria-stabilized zirconia (YSZ), which can be a suitable electrolyte of solid oxide fuel cell [1]. The diffusion of oxide ions through oxygen vacancy is enhanced by doping of $Sr^{2+}$ and $Mg^{2+}$ ions into $La^{3+}$ and $Ga^{3+}$ sites, respectively. The substitution of divalent cation for trivalent cation produces oxygen vacancy because of the charge neutrality ($2SrO \xrightarrow{La_2O_3} 2Sr'_{La} + 2O^{\times}_{O} + \ddot{V}_O$). However, Ga content of igneous rock, on average, is only 15 ppm and Ga is an expensive element for industrial applications. In our previous paper [2], perovskite solid solutions of $(La_{0.6}Sr_{0.4})(X_{1-y}Mg_y)O_{3-\delta}$ with stable valence of A and B site cations were synthesized for the abundant elements of X = Al, Ti and Zr. Single phase perovskite solid solutions (for example, $(La_{0.6}Sr_{0.4})(Zr_{0.6}Mg_{0.4})O_{2.9}$ or $(La_{0.6}Sr_{0.4})(Al_{0.9}Mg_{0.1})O_{2.75}$) were produced for the lattice oxide ion compositions $(3-\delta) < 3$ upon heating at 1000–1500 °C in air. The oxide systems with lattice oxide ion compositions of $(3-\delta) > 3$ decomposed into several phases. $(La_{0.6}Sr_{0.4})(Al_{0.9}Mg_{0.1})O_{2.75}$ (shorten as LSAM) with a relative density of 99.1% showed a relatively high electrical conductivity of $4.15 \times 10^{-4}$ S/cm at 600 °C [2]. In this paper, $(La_{1-x}Sr_x)(Al_{1-y}Mg_y)O_{3-\delta}$ perovskite solid solutions ($x = 0$–$0.4$, $y = 0$–$0.3$) were prepared to examine the influence of substitution of A site and B site cations on its electrical conductivity in air at 300–800 °C. The measured results indicate that (1) the sinterability of LSAM solid solutions is controlled by the diffusion rate of A site cations, (2) a long heating at a high temperature is needed to prepare dense LSAM because of the relatively low diffusion rates of $La^{3+}$ and $Sr^{2+}$ ions in LSAM, and (3) the highest electrical conductivity and the lowest activation energy are achieved at the compositions of $x = 0.2$ and $y = 0.1$. Although $(La_{0.8}Sr_{0.2})(Al_{0.9}Mg_{0.1})O_{2.85}$ electrolyte sintered at 1400 °C for 12 h contained 28% porosity, its conductivity was higher than the conductivity of dense 8 mol% YSZ used widely as an oxide ion electrolyte for solid oxide fuel cell and oxygen gas sensor. This paper

* Corresponding author. Tel.: +81 99 285 8325; fax: +81 99 257 4742.
*E-mail address:* hirata@apc.kagoshima-u.ac.jp (Y. Hirata).

Peer review under responsibility of The Ceramic Society of Japan and the Korean Ceramic Society.

Production and hosting by Elsevier

2187-0764 © 2014 The Ceramic Society of Japan and the Korean Ceramic Society. Production and hosting by Elsevier B.V. All rights reserved.
http://dx.doi.org/10.1016/j.jascer.2014.03.005

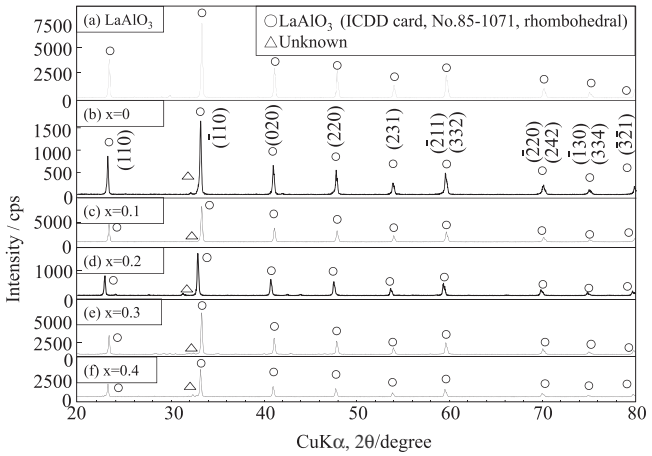


**Fig. 1.** X-ray diffraction patterns of (a) $LaAlO_3$ and $(La_{1-x}Sr_x)(Al_{0.9}Mg_{0.1})O_{3-\delta}$ solid solution with (b) $x = 0$, (c) $x = 0.1$, (d) $x = 0.2$, (e) $x = 0.3$ and (f) $x = 0.4$, heated at 1500 °C in air.

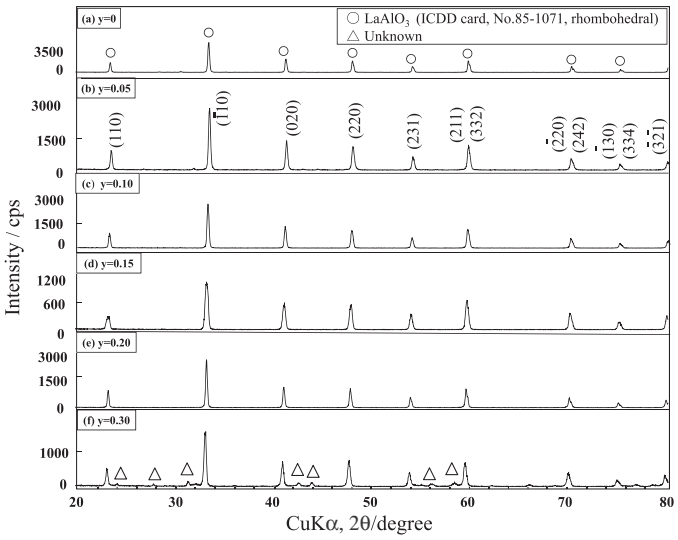


**Fig. 2.** X-ray diffraction patterns of LSAM with $(La_{0.8}Sr_{0.2})(Al_{1-y}Mg_y)O_{3-\delta}$ composition ($y = 0$–0.3) after two step heating: 1st heating at 1500 °C for 10 h in LSAM powder preparation and subsequent heating of 1400 °C for 12 h for sintering.

reports a detailed study of powder preparation, sintering behavior, sintered microstructures, lattice parameter, and electrical conductivity for $(La_{1-x}Sr_x)(Al_{1-y}Mg_y)O_{3-\delta}$ system as an alternative oxide ion conductor.

## 2. Experimental procedure

LSAM solid solution powders with $x = 0$–0.4 at $y = 0.1$ and $y = 0$–0.3 at $x = 0.2$ in $(La_{1-x}Sr_x)(Al_{1-y}Mg_y)O_{3-\delta}$ were prepared by heating the precursor precipitate [2–4]. Aqueous solutions (0.2 M) of $La(NO_3)_3{\cdot}6H_2O$ (purity > 99.9 mass%), $Sr(NO_3)_2$ (purity > 98 mass%), $Al(NO_3)_3{\cdot}9H_2O$ (purity > 99.9 mass%) and $Mg(NO_3)_2{\cdot}6H_2O$ (purity > 99 mass%) were mixed at the molar ratios of $La/Sr/Al/Mg = (1-x)/x/(1-y)/y$. The mixed metal aqueous solution was added into a stirred 0.2 M $(NH_4)_2CO_3$ solution to form carbonate coprecipitate. The freeze-dried powder was heated at 1500 °C for 10 h in air. The phases produced in heated powders were identified by X-ray diffraction (RINT 2200, Rigaku Co. Ltd., Japan). The lattice parameter of heated LSAM powder with high purity Si as an internal standard was measured. The heated LSAM powders were compacted by uniaxial pressing at 49 MPa, followed by cold isostatic pressing at 294 MPa to a disk with sizes of 10 mm diameter and 2 mm thickness. The compacts were sintered at 1400 °C for 12 h in air and the sintered densities were measured by the Archimedes method using kerosene. The microstructures of surface of sintered compacts were observed by a scanning electron microscope (SM-300, Topcon Co., Tokyo, Japan). Au paste was spread homogeneously on the surfaces of sintered LSAM and heated at 850 °C for 2 h to achieve an ohmic contact between the sintered LSAM sample and electrode. Furthermore, two Pt plates with Pt wires were attached to the Au electrodes to measure the AC impedance of LSAM sample. The electrical conductivity of LSAM was measured in the temperature range from 300 to 800 °C by a two-terminal AC bridge at 100 Hz–2 MHz (E4980A, Agilent Technologies Inc., USA).

## 3. Results and discussion

### 3.1. Formation of LSAM solid solution

Fig. 1 shows the X-ray diffraction patterns of $LaAlO_3$ plus $(La_{1-x}Sr_x)(Al_{0.9}Mg_{0.1})O_{3-\delta}$ ($x = 0$–0.4) heated at 1500 °C for 10 h in air. All the diffraction patterns of $LaAlO_3$ and LSAM were referred to a rhombohedral structure (ICCD card, No. 85-1071). Some unknown small peaks were recognized but they were not from the diffraction patterns of $La_2O_3$, SrO, $Al_2O_3$, MgO or $MgAl_2O_4$. The above result suggests that the combination of carbonate coprecipitation method and freeze drying for the precursor metal solutions is effective to prepare LSAM solid solution. Fig. 2 shows the X-ray diffraction patterns for LSAM with $(La_{0.8}Sr_{0.2})(Al_{1-y}Mg_y)O_{3-\delta}$ composition ($y = 0$–0.3) after two-step heating: 1st heating of 1500 °C for 10 h in LSAM powder preparation and subsequent 2nd heating of 1400 °C for 12 h for LSAM sintering. It was possible to index all the diffraction peaks as a rhombohedral structure. As seen in Fig. 2(f), some unknown small peaks were also recognized at the composition of $y = 0.3$. These unknown small peaks appeared at the other compositions after the 1st heating but they disappeared by further 2nd heating. This result indicates that a long heating at a high temperature is needed to achieve a complete LSAM solid solution because of the relatively low diffusion coefficients of the constitutive atoms.

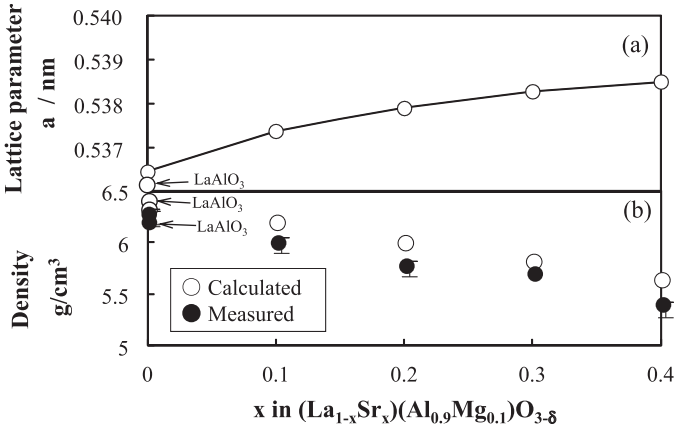


**Fig. 3.** (a) Lattice parameters for LSAM with $(La_{1-x}Sr_x)(Al_{0.9}Mg_{0.1})O_{3-\delta}$ composition in Fig. 1 and (b) calculated density and measured apparent density for LSAM sintered at 1400 °C for 12 h.

Fig. 3 shows (a) the lattice parameters for LSAM with $(La_{1-x}Sr_x)(Al_{0.9}Mg_{0.1})O_{3-\delta}$ composition in Fig. 1 and (b) the calculated density using the lattice parameter and the apparent density measured by the Archimedes method for the LSAM sintered at

1400 °C for 12 h. The lattice parameter in Fig. 3(a) increased nonlinearly with increasing Sr content. The change in the lattice parameter in Fig. 3(a) is explained by the difference of ionic radii of $La^{3+}$ (0.136 nm of ionic radius for coordination number 12), $Sr^{2+}$ (0.144 nm of ionic radius for coordination number 12), $O^{2-}$ (0.140 nm of ionic radius for coordination number 6) [5] and oxygen vacancy (ionic radius: 0.1164 nm for rare earth-doped ceria and 0.0993 nm for rare earth-stabilized zirconia for coordination number 4) [6]. The ionic radius of oxygen vacancy in $LaAlO_3$ perovskite solid solution is discussed in Section 3.5 and Appendix A. The substitution of larger $Sr^{2+}$ ions for smaller $La^{3+}$ ions is accompanied by the formation of oxygen vacancy to maintain the charge neutrality. The size of oxygen vacancy is reported to be smaller than the size of oxide ion [6]. The calculated radius of oxygen vacancy in perovskite structure showed a difference between A site substitution and B site substitution, and was larger for A site substitution (0.1072 nm) than for B site substitution (0.0443 nm). The above size relations at A site and oxide ion lattice site result in the measured change of lattice parameter in Fig. 3(a). According to our previous experiment [2], the formation of single phase LSAM solid solution was also recognized at $x = 0.4$ composition, indicating that $Sr^{2+}$ ions can be substituted for $La^{3+}$ ions in the wide range of composition of A site. This result is due to the similar sizes of $La^{3+}$ and $Sr^{2+}$ ions. Nguyen et al. also reported that the lattice parameter of $(La_{1-x}Sr_x)AlO_{3-\delta}$ ($x = 0$–0.2) assigned as a hexagonal structure expands linearly with increasing $x$ value [7]. The measured apparent density of LSAM containing closed pores in Fig. 3(b) was close to the calculated true density, suggesting that little closed pores were formed in the sintered LSAM solid solution. The ratios (0.93–0.95) of apparent density (containing closed pores) to true density were independent of $x$ value. The lattice parameter of $LaAlO_3$ was slightly smaller than that of $La(Al_{0.9}Mg_{0.1})O_{2.95}$. Substitution of $Mg^{2+}$ ions (0.072 nm of ionic radius for coordination number 6) for $Al^{3+}$ ions (0.0535 nm of ionic radius for coordination number 6) at B site causes the increase of lattice parameter. The formation of oxygen vacancy is also accompanied by the substitution of $Mg^{2+}$ ions for $Al^{3+}$ ions and decreases the lattice parameter because of the size relationship of oxygen vacancy and oxide ion. The experimental result suggests that the overall effects of B site cations and oxide ion lattice site provide little change of lattice parameters between $LaAlO_3$ and $La(Al_{0.9}Mg_{0.1})O_{2.95}$.

Fig. 4 shows (a) the lattice parameters for LSAM with $(La_{0.8}Sr_{0.2})(Al_{1-y}Mg_y)O_{3-\delta}$ composition in Fig. 2 and (b) the calculated and measured apparent densities for LSAM sintered at 1400 °C for 12 h. The lattice parameter of $(La_{0.8}Sr_{0.2})(Al_{1-y}Mg_y)O_{3-\delta}$ increased linearly with $y$ value and reached a constant value of 0.5369 nm at $y = 0.15$, indicating the solubility of $Mg^{2+}$ ions into Al

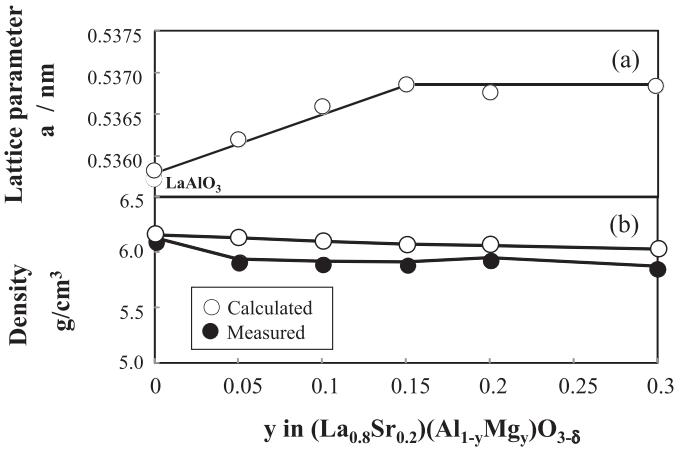


**Fig. 4.** (a) Lattice parameters for LSAM with $(La_{0.8}Sr_{0.2})(Al_{1-y}Mg_y)O_{3-\delta}$ composition in Fig. 2 and (b) calculated density and measured apparent density for LSAM sintered at 1400 °C for 12 h.

site. Although no second phase was detected at $y = 0.2$ composition in Fig. 2, the result in Fig. 4(a) suggests that a small amount of excess MgO may form the unknown phase below the amount of detection limit by X-ray diffraction. As compared with the substitution at A site with $Sr^{2+}$ ions for $La^{3+}$ ions, the solubility of $Mg^{2+}$ ions substituted at B site was small. This result is due to the relatively large difference of sizes between $Mg^{2+}$ ions (ionic radius 0.072 nm of ionic radius for coordination number 6) and $Al^{3+}$ ions (ionic radius 0.0535 nm of ionic radius for coordination number 6). The change of calculated density with $y$ value was small and a similar tendency was also measured for the apparent density. It is noted that the solubility limit of $Mg^{2+}$ ions was $y = 0.15$ and the true densities by X-ray diffraction at $y = 0.2$ and $y = 0.3$ compositions were approximated as a single phase solid solution. The difference of composition dependence of measured apparent density on $x$ (Fig. 3) and $y$ values (Fig. 4) is explained by the difference of atomic weights of metals at A and B sites under the same condition for the formation of oxygen vacancy. The larger difference of atomic weights at A site (La: 138.905, Sr: 87.621) causes the significant change in the density (Fig. 3). However, the smaller difference of atomic weights for Al (29.981) and Mg (24.305) at B site provides the small change in the density (Fig. 4).

### 3.2. Microstructures of sintered LSAM

Fig. 5 shows the microstructures of $LaAlO_3$ and $(La_{1-x}Sr_x)(Al_{0.9}Mg_{0.1})O_{3-\delta}$ sintered at 1400 °C for 12 h in air.

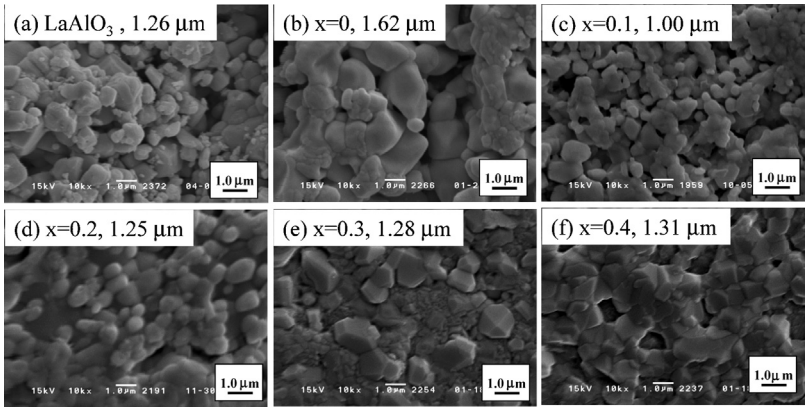


**Fig. 5.** Microstructures of $LaAlO_3$ (a) and $(La_{1-x}Sr_x)(Al_{0.9}Mg_{0.1})O_{3-\delta}$ (b–f) sintered at 1400 °C.

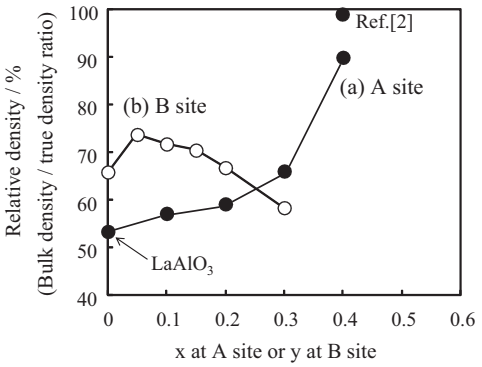


**Fig. 6.** Composition dependence of relative density of $(La_{1-x}Sr_x)(Al_{0.9}Mg_{0.1})O_{3-\delta}$ and $(La_{0.8}Sr_{0.2})(Al_{1-y}Mg_y)O_{3-\delta}$ sintered at 1400 °C for 12 h in air.

The microstructures of $LaAlO_3$ and $(La_{1-x}Sr_x)(Al_{0.9}Mg_{0.1})O_{3-\delta}$ consisted of equiaxis grains and the average grain size was not affected by the Sr composition. The ratios of measured bulk density (including closed and open pores) to the calculated true density for the observed microstructures were plotted in Fig. 6, and 53.4%, 57.2%, 59.2%, 66.1% and 90.0% for $LaAlO_3$ and LSAM at $x = 0.1$, 0.2, 0.3 and 0.4, respectively. The relative density at the composition $x = 0.4$ after sintering at 1500 °C for 12 h was 99.1% in our previous paper [2]. As seen in Fig. 6, the sinterability of LSAM depends greatly on the A site composition and increases above 0.3 of $x$ value. The substitution of slightly larger $Sr^{2+}$ ions for slightly smaller $La^{3+}$ ions increases the unit cell size (Fig. 3) and enhances the migration rate of A site cations during heating, which control the sintering rate.

Fig. 7 shows the microstructures of $(La_{0.8}Sr_{0.2})(Al_{1-y}Mg_y)O_{3-\delta}$ sintered at 1400 °C for 12 h in air. The ratios of measured bulk density (including closed and open pores) to the calculated true density for the microstructures in Fig. 7 were also plotted in Fig. 6, and 65.9%, 73.8%, 71.8%, 70.5%, 66.8% and 58.4% for $y = 0$, 0.05, 0.1, 0.15, 0.2 and 0.3 in $(La_{0.8}Sr_{0.2})(Al_{1-y}Mg_y)O_{3-\delta}$, respectively. As seen in Fig. 6, the substitution of larger $Mg^{2+}$ ions for smaller $Al^{3+}$ ions at B site showed a maximum of relative density at $y = 0.05$ composition, and caused a decrease in the sinterability at a higher $y$ value. The observed microstructures reflect well the change in the bulk density. Little grain growth was measured in the porous microstructures below 70% relative density at $y = 0$, 0.2 and 0.3 compositions. The microstructures became denser at $y = 0.05$, 0.1 and 0.15 compositions with relative density of 70–74%. The bulk density with B site substitution in Fig. 6 is an opposite tendency against the density change with A site substitution. The above two types of trend of density in Fig. 6 are interpreted that the diffusion of A site cations, which controls the sintering rate of LSAM solid solution, is suppressed owing to the increased volume of B site upon the substitution of larger $Mg^{2+}$ ions for smaller $Al^{3+}$ ions. That is, the sinterability of LSAM solid solution is increased by increasing the Sr composition at A site and by decreasing the Mg composition at B site.

### 3.3. Electrical conductivity of $(La_{1-x}Sr_x)(Al_{0.9}Mg_{0.1})O_{3-\delta}$

Although the present LSAM solid solutions were not a dense material as seen in Fig. 6, the measured conductivities were comparable to the conductivity of dense CSZ (calcia-stabilized zirconia) or YSZ electrolyte. This section focusses on the characteristics of electrical conductivity of porous LSAM electrolyte. When a dense LSAM solid solution was prepared by hot-pressing, more detailed results may be discussed in a future paper. Fig. 8 shows the complex impedance plots at (a) $x = 0.1$, (b) $x = 0.2$, (c) $x = 0.3$ and (d) $x = 0.4$ for $(La_{1-x}Sr_x)(Al_{0.9}Mg_{0.1})O_{3-\delta}$ in air at 400 °C. The impedance plot expresses a distorted semicircle which is related to the multi-relaxation of migration of oxide ions. The degree of multi-relaxation was evaluated by the angle $\theta$ is shown in Fig. 8. The semicircle at the high frequency range ($R_1$) and the low frequency range ($R_2$) may represent the bulk and gain boundary resistance, respectively. Fig. 9 shows the influence of $x$ value on (a) angle $\theta$ and (b) the ratio of grain boundary resistance ($R_2$) to total resistance (bulk resistance ($R_1$) plus grain boundary resistance ($R_2$)). The angle $\theta$ at $x = 0$–0.3 was almost constant at 400–600 °C but the angle $\theta$ at $x = 0.4$ became larger. The standard deviation of grain size distribution was 0.33–0.47 μm at $x = 0$–0.3 but increased to 0.64 μm at $x = 0.4$. The larger angle $\theta$ at $x = 0.4$ may result from the larger standard deviation of grain size. The grain boundary resistance ($R_2$) dominates the sample resistance at 400 °C. On the other hand, the fraction of grain boundary resistance ($R_2$) at 600 °C showed a minimum value at $x = 0.2$. This result is related to the composition dependence of the conductivity in Fig. 10.

Fig. 10 shows the Arrhenius plots of total electrical conductivities of $(La_{1-x}Sr_x)(Al_{0.9}Mg_{0.1})O_{3-\delta}$ ($x = 0$–0.4), $LaAlO_3$ and related oxide ion conductors [1,2,8–10]. The conductivity of $LaAlO_3$ was low because of no formation of oxygen vacancy. The conductivity of LSAM showed the highest value at $x = 0.2$ ($1.86 \times 10^{-3}$ S/cm at 600 °C). This value was higher than that of 15 mol% calcia-stabilized zirconia (CSZ) and was close to that of 8 mol% YSZ. When the composition $x$ was increased to $x = 0.3$ and 0.4, the conductivity of LSAM decreased. The electrical conductivity of dense $(La_{0.6}Sr_{0.4})(Al_{0.9}Mg_{0.1})O_{3-\delta}$ (99.1% of relative density) is also plotted in Fig. 10 [2]. The conductivity ($4.15 \times 10^{-4}$ S/cm at 600 °C)

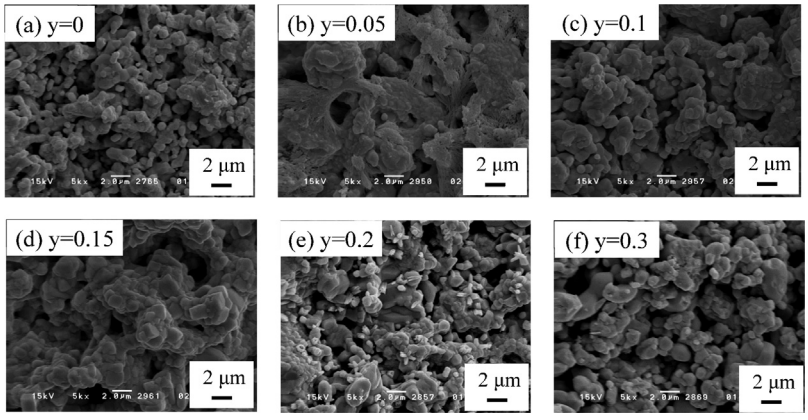


**Fig. 7.** Microstructures of $(La_{0.8}Sr_{0.2})(Al_{1-y}Mg_y)O_{3-\delta}$ sintered at 1400 °C.

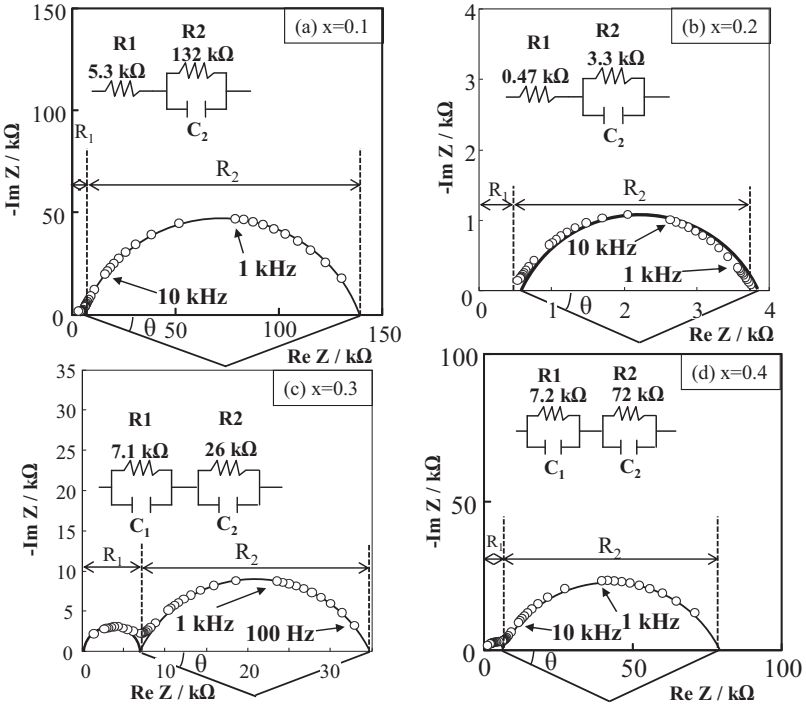


**Fig. 8.** Complex impedance plots of $(La_{1-x}Sr_x)(Al_{0.9}Mg_{0.1})O_{3-\delta}$ with (a) $x = 0.1$, (b) $x = 0.2$, (c) $x = 0.3$ and (d) $x = 0.4$ in air at 400 °C.

of dense LSAM at $x = 0.4$ was higher than that of porous LSAM of 90.0% of relative density ($0.95 \times 10^{-4}$ S/cm at 600 °C). It is noted that the conductivity of porous LSAM at $x = 0.2$ is still higher than that of dense LSAM at $x = 0.4$. In Fig. 10, the electrical conductivities of $LaAlO_3$ and $(La_{0.9}Sr_{0.1})(Al_{0.9}Mg_{0.1})O_{2.9}$ (relative densities were not shown) measured by Chen et al. [10] are also plotted by dotted lines. Their data for the samples sintered at 1600 °C for 3 h were slightly higher than the present conductivities. As seen in Fig. 10, the Arrehenius plots of the conductivities at $x = 0$, 0.2, 0.3 and 0.4 were expressed by one straight line but the composition of $x = 0.1$ provided the bent of the Arrhenius plot at 500 °C. Schneider et al. [11] and Inaba et al. [12] have reported a phase transition of $LaAlO_3$ from rhombohedral to cubic phase at 440 and 527 °C, respectively, with increasing temperature.

A similar phase transition in $(La_{0.9}Sr_{0.1})(Ga_{0.8}Mg_{0.2})O_{2.85}$ is also observed at 700 °C in Fig. 10. However, no bent of the Arrhenius plot for the present $LaAlO_3$ was measured in the wide temperature range of 300–800 °C. The above measured result is discussed more in Section 3.4. The activation energy of the electrical conductivity was 103.0, 153.7, 101.9, 113.3 and 104.4 kJ/mol for $LaAlO_3$, $x = 0$, $x = 0.2$, $x = 0.3$ and $x = 0.4$ of LSAM, respectively. The activation energy of LSAM at $x = 0.1$ composition was 113.8 and 159.3 kJ/mol in the high and low temperature range, respectively. The above results are summarized as follows: (1) the activation energy was comparable (102–113 kJ/mol) in the wide composition range of LSAM including the high temperature range at $x = 0.1$ composition, and (2) a relative high activation energy (154–159 kJ/mol) was measured at $x = 0$ and in the low temperature range at $x = 0.1$ composition. The activation energy of dense LSAM at $x = 0.4$ in Ref. [2] is 113.4 kJ/mol and close to that of porous LSAM at $x = 0.4$ in

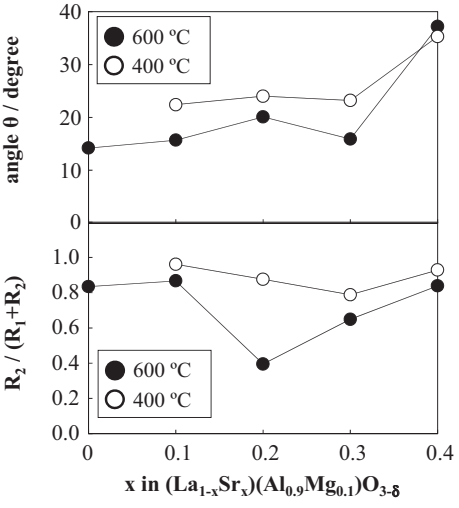


**Fig. 9.** Influence of composition of $(La_{1-x}Sr_x)(Al_{0.9}Mg_{0.1})O_{3-\delta}$ on (a) angle $\theta$ and (b) ratio of grain boundary resistance ($R_2$) to total resistance ($R_1 + R_2$).

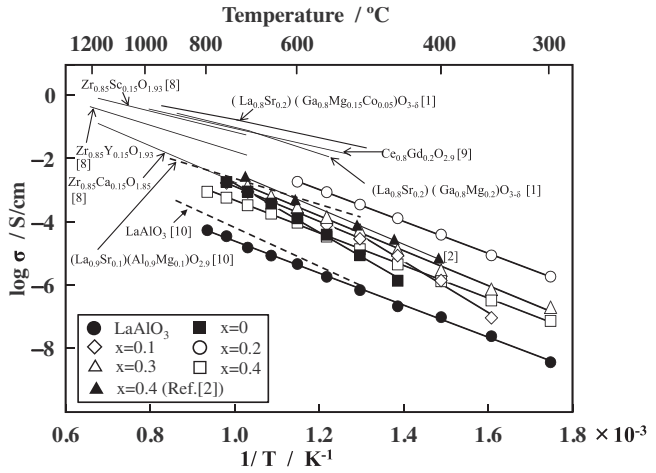


**Fig. 10.** Arrhenius plots of electrical conductivities of $(La_{1-x}Sr_x)(Al_{0.9}Mg_{0.1})O_{3-\delta}$ solid solution and related oxide ion conductors in air.

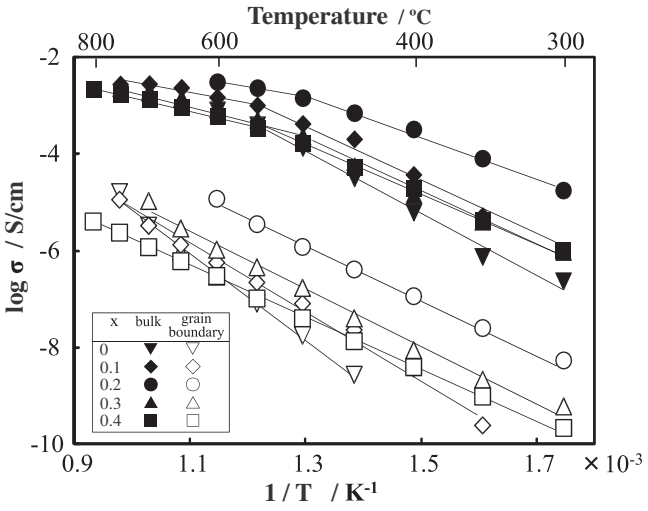


**Fig. 11.** Arrhenius plots of bulk and grain boundary conductivities of $(La_{1-x}Sr_x)(Al_{0.9}Mg_{0.1})O_{3-\delta}$ solid solution.

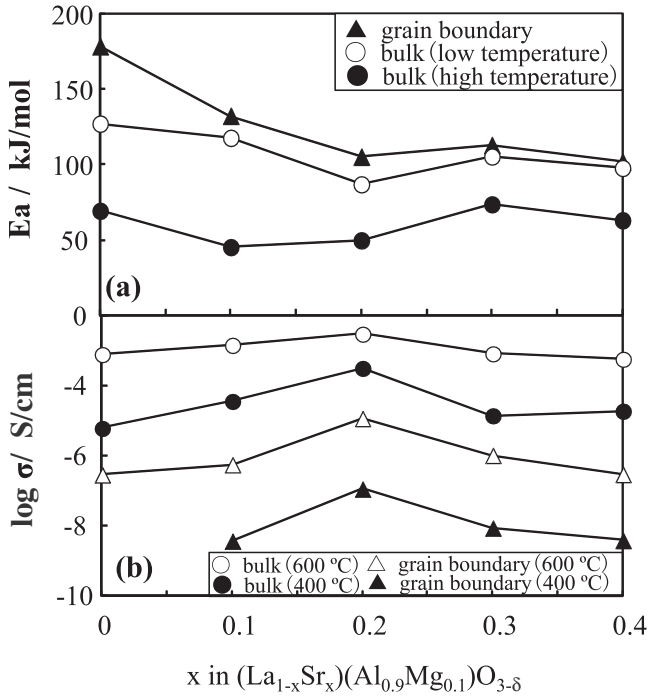


**Fig. 12.** (a) Activation energy and (b) electrical conductivity of bulk and grain boundary conduction of $(La_{1-x}Sr_x)(Al_{0.9}Mg_{0.1})O_{3-\delta}$ solid solution.

this study. The activation energy of LSAM with the highest conductivity at $x = 0.2$ is higher than that of $(La_{0.8}Sr_{0.2})(Ga_{0.8}Mg_{0.2})O_{2.80}$ (54 kJ/mol) [1] or $Ce_{0.8}Gd_{0.2}O_{1.9}$ (79 kJ/mol) [9] but is comparable to that of 8 mol% YSZ (96 kJ/mol) [8] or 15 mol% CSZ (114 kJ/mol) [8].

### 3.4. Bulk conductivity and grain boundary conductivity of $(La_{1-x}Sr_x)(Al_{0.9}Mg_{0.1})O_{3-\delta}$

In our previous paper, the thickness of grain boundary for Gd-doped ceria was estimated to be 2–7 nm for the microstructures with average grain sizes of 0.29–5.6 μm [13]. In this paper, the grain boundary conductivity of LSAM was calculated under the assumption of 3 nm of grain boundary thickness at a given average grain size (Fig. 5). Fig. 11 shows the Arrhenius plots of bulk and grain boundary conductivities of LSAM. The bulk conductivity was 100–1000 times as high as the grain boundary conductivity. The bulk conductivity showed a bent at 500–550 °C but the Arrhenius plot of the grain boundary conductivity was represented by one straight line. This result may suggest that the bent in the bulk conductivity is related to the structure change from rhombohedral (low temperature range) to cubic structure (high temperature range). The experimental confirmation of the high temperature structure of LSAM is to be studied in near future. The bulk conductivity, grain boundary conductivity and their activation energies are summarized in Fig. 12. The interesting result is that both the bulk and grain boundary conductivities showed a maximum at $x = 0.2$ in $(La_{1-x}Sr_x)(Al_{0.9}Mg_{0.1})O_{3-\delta}$. The flux of oxide ions across grain boundary may be strongly affected by the flux of oxide ions within bulk. The gradual increase of the bulk conductivity at $x = 0$–$0.2$ is caused by the increased concentration of oxygen vacancy with substitution of $Sr^{2+}$ ions for $La^{3+}$ ions. The decrease of the bulk conductivity at $x > 0.2$ may result from the strong interaction between too many positively charged oxygen vacancy and too many negatively charged $Sr'_{La}$ sites, which suppresses the migration of oxide ions through oxygen vacancy.

The composition dependence of both the activation energies showed an opposite tendency against the composition dependence of the bulk conductivity. That is, the composition of $x = 0.2$ of LSAM provides the highest conductivity and the lowest activation energy. Park and Choi [14] report the electrical conductivity and activation energy of bulk conductivity for $(La_{0.9}Sr_{0.1})(Al_{0.9}Mg_{0.1})O_{2.9}$. Their bulk conductivity at 600 °C is $1.26 \times 10^{-3}$ S/cm and comparable to the value of $1.47 \times 10^{-3}$ S/cm in this experiment. The activation energy reported by Park and Choi is 100.3 kJ/mol at 400–600 °C and 45.3 kJ/mol at 600–800 °C, respectively. These values are similar to the activation energy in Fig. 12.

### 3.5. Electrical conductivity of $(La_{0.8}Sr_{0.2})(Al_{1-y}Mg_y)O_{3-\delta}$

Since the influence of A site composition on the conductivity of LSAM sold solution was high at $x = 0.2$ composition in Fig. 10, the effect of B site composition on the conductivity was examined under the fixed composition of $x = 0.2$ of A site. Fig. 13 shows the complex impedance plots at (a) $y = 0$, (b) $y = 0.05$, (c) $y = 0.15$ and (d) $y = 0.20$ for $(La_{0.8}Sr_{0.2})(Al_{1-y}Mg_y)O_{3-\delta}$ in air at 600 °C. The impedance plots were similar to those for $(La_{1-x}Sr_x)(Al_{0.9}Mg_{0.1})O_{3-\delta}$ in Fig. 8 and consisted of two semicircles. The grain boundary resistance represented by the semicircle in the low frequency range ($R_2$) dominated the total resistance ($R_1 + R_2$) at all the compositions. Fig. 14 shows the Arrhenius plots of electrical conductivity for $(La_{0.8}Sr_{0.2})(Al_{1-y}Mg_y)O_{3-\delta}$. The conductivity increased with an increase in $y$ value up to 0.10 but showed a similar lower value at $y = 0.15$, 0.20 and 0.30. The composition dependence of conductivity in Figs. 10 and 14 indicates that LSAM solid solution of $(La_{0.8}Sr_{0.2})(Al_{0.9}Mg_{0.1})O_{3-\delta}$ composition possesses the highest electrical conductivity. As seen in Fig. 14, the conductivities of present LSAM at $y = 0$–$0.1$ are comparable to the conductivity of 8 mol% YSZ [8] and lower than the conductivity of $Ce_{0.8}Gd_{0.2}O_{1.9}$ [9] or $(La_{0.8}Sr_{0.2})(Ga_{0.8}Mg_{0.2})O_{3-\delta}$ [1]. It is noted that the present LSAM at $y = 0.1$ possesses a higher conductivity of $6.79 \times 10^{-3}$ S/cm at 600 °C than dense $(La_{0.9}Sr_{0.1})(Al_{0.97}Mg_{0.03})O_{3-\delta}$ (95% relative density, $1.56 \times 10^{-3}$ S/cm at 600 °C) in Ref. [15].

The apparent activation energy of electrical conductivity was 101.8, 94.4, 98.8, 118.9, 141.4 and 143.0 kJ/mol at $y = 0$, 0.05, 0.10, 0.15, 0.20 and 0.30 in $(La_{0.8}Sr_{0.2})(Al_{1-y}Mg_y)O_{3-\delta}$, respectively. The small $y$ values of $y = 0$–$0.10$ gave the low apparent activation energy

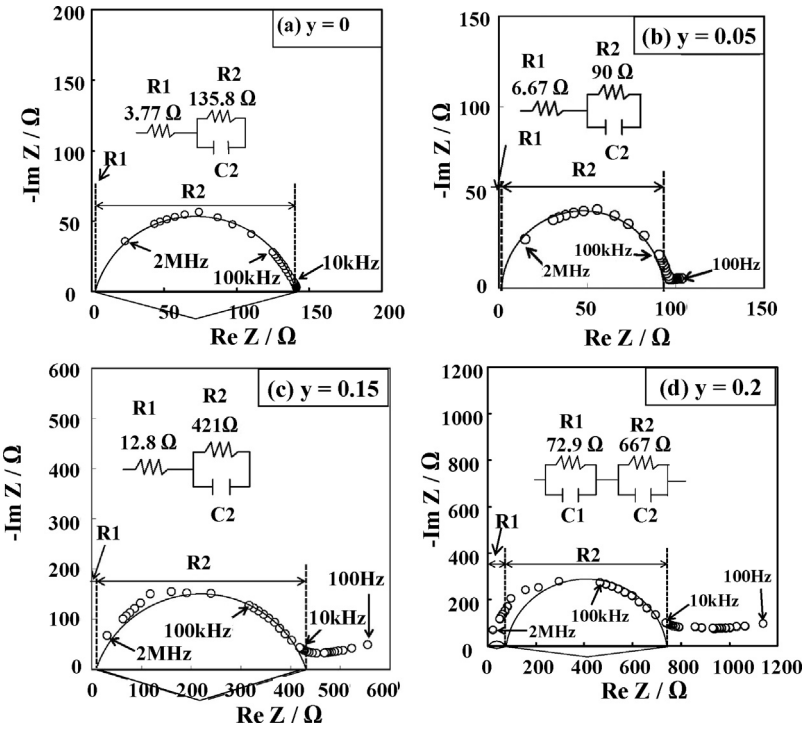


**Fig. 13.** Complex impedance plots of $(La_{0.8}Sr_{0.2})(Al_{1-y}Mg_y)O_{3-\delta}$ with (a) $y = 0$, (b) $y = 0.05$, (c) $y = 0.15$ and (d) $y = 0.2$.

but an increase in $y$ value to 0.15–0.30 resulted in the higher activation energy. The increase in the concentration of oxygen vacancy and the increased volume of B site (Figs. 4 and 6) with increasing $y$ value affect the diffusion of oxide ions through the vacancy mechanism. Fig. 15 shows (a) the conductivity and (b) the apparent activation energy at 600 °C for LSAM solid solutions as a function of oxide ion composition $(3-\delta)$. The conductivity with $x$ composition at A site and with $y$ composition at B site showed a similar maximum value at the oxide ion composition of $3-\delta = 2.85$. The increase of the conductivity in the range of $3-\delta = 2.95$–$2.85$ reflects the increased concentration of available oxygen vacancy for the diffusion of oxide ions. The decreased conductivity in the range of $3-\delta = 2.85$–$2.75$ may be related to the strong association of too many positively charged oxygen vacancy and too many negatively charged $Sr'_{La}$ sites or $Mg'_{Al}$ sites, because the concentrations of these defects increase with $x$ or $y$ value. An interesting result is the opposite tendency of the activation energy with oxide ion composition. Both the activation energies dropped at the composition of $3-\delta = 2.85$ where the conductivity became a maximum.

The conductivity and activation energy shown in Fig. 15 also include the influence of structural strain with the formation of LSAM solid solution. The structural deviation from an ideal cubic structure in perovskite oxide is expressed by Eq. (1) (tolerance factor)

$$t = \frac{(r_A + r_O)}{\sqrt{2}(r_B + r_O)} \quad (1)$$

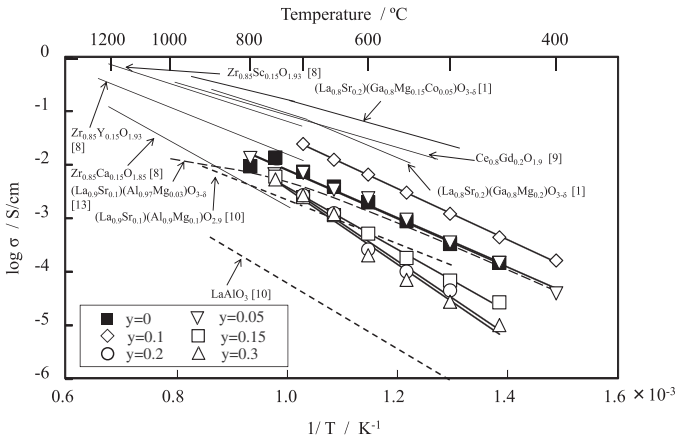


**Fig. 14.** Arrhenius plots of electrical conductivities of $(La_{0.8}Sr_{0.2})(Al_{1-y}Mg_y)O_{3-\delta}$ solid solution and related oxide ion conductors in air.

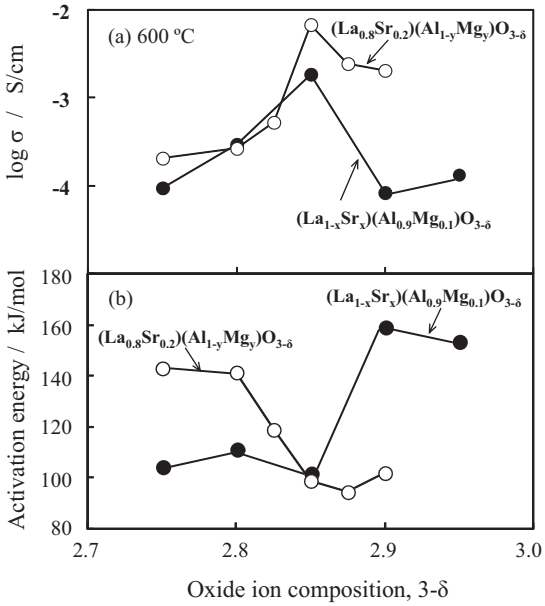


**Fig. 15.** (a) Conductivity and (b) activation energy at 600 °C for LSAM as a function of oxide ion composition $(3-\delta)$.

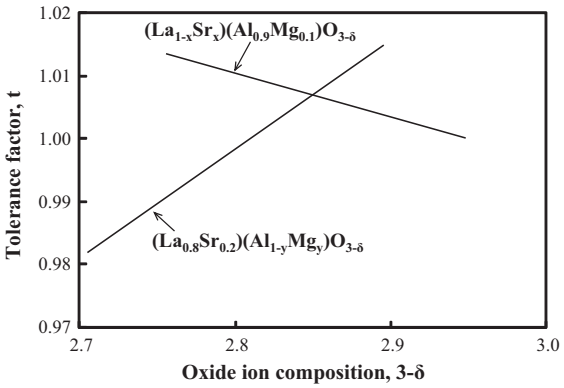


**Fig. 16.** Relationship between tolerance factor and oxide ion composition for LSAM solid solution.

where $r_A$ is the ionic radius of A site cation, $r_B$ is the ionic radius of B site cation and $r_O$ is the ionic radius of oxide ion. As the tolerance factor decreases, the structure of unit cell changes from cubic to rhombohedral structure. The $t$ value by Eq. (1) for present $(La_{1-x}Sr_x)(Al_{1-y}Mg_y)O_{3-\delta}$ perovskite solid solution was calculated using the following average ionic radii:

$$r_A\,(\text{coordination number } 12) = (1-x)r_{La^{3+}}(0.136\,\text{nm}) + x r_{Sr^{2+}}(0.144\,\text{nm}) \quad (2)$$

$$r_B\,(\text{coordination number } 6) = (1-y)r_{Al^{3+}}(0.0535\,\text{nm}) + y r_{Mg^{2+}}(0.072\,\text{nm}) \quad (3)$$

$$r_O\,(\text{coordination number } 6) = \left[(3-\delta)/3\right] r_{O^{2-}}(0.140\,\text{nm}) + \left[\delta/3\right] r_{\ddot{V}_O}(0.1072\,\text{nm}) \quad (4)$$

Fig. 16 shows the relationship between tolerance factor and oxide ion composition for LSAM solid solution using 0.1072 nm of ionic radius of oxygen vacancy for A site substitution (see Appendix A for the size of oxygen vacancy). The $t$ values for $(La_{1-x}Sr_x)(Al_{0.9}Mg_{0.1})O_{3-\delta}$ and $(La_{0.8}Sr_{0.2})(Al_{1-y}Mg_y)O_{3-\delta}$ show an opposite tendency as the oxide ion composition increases. The two lines cross at $3-\delta = 2.85$ where $t$ value becomes 1.007. This cross point corresponds at $x = 0.2$ and $y = 0.1$. That is, the formation of perovskite solid solution with the smaller structural strain is another factor for the highest electrical conductivity and the lowest activation energy as shown in Fig. 15.

## 4. Summary

Perovskite solid solution $(La_{1-x}Sr_x)(Al_{1-y}Mg_y)O_{3-\delta}$ compositions ($x = 0$–$0.4$ and $y = 0$–$0.3$, shortened as LSAM) were produced from the freeze-dried precursor carbonate coprecipitate by heating at 1500 °C for 10 h and subsequent sintering at 1400 °C for 12 h in air. The produced LSAM solid solutions inherited the mother structure of rhombohedral $LaAlO_3$. The change of lattice parameter with $x$ or $y$ value suggests the formation of solid solution in the range of $x = 0$–$0.4$ at $y = 0.1$ and in the range of $y = 0$–$0.15$ at $x = 0.2$. The sinterability of LSAM was dominated by the composition of A site cations and increased above 0.3 of $x$ value. The substitution of slightly larger $Sr^{2+}$ ions for slightly smaller $La^{3+}$ ions increases the unit cell size and enhances the migration rate of A site cations during heating. However, the diffusion of A site cations is suppressed owing to the increased volume of B site upon the substitution of larger $Mg^{2+}$ ions for smaller $Al^{3+}$ ions. That is, the sinterability of LSAM solid solution is increased by increasing the Sr composition at A site and by decreasing the Mg composition at B site. The electrical conductivity of the present porous LSAM solid solutions with 26–42% porosity was dominated by the grain boundary resistance. The conductivity with $x$ composition at A site and with $y$ composition at B site showed a similar maximum value at the oxide ion composition of $3-\delta = 2.85$ ($(La_{0.8}Sr_{0.2})(Al_{0.9}Mg_{0.1})O_{2.85}$). This result reflects the effects of three factors: concentration of available oxygen vacancy, association of positively charged oxygen vacancy and negatively charged $Sr'_{La}$ sites or $Mg'_{Al}$ sites and structural strain of solid solution. Both the activation energies with A site substitution and B site substitution decreased at the oxide ion composition of $3-\delta = 2.85$. This composition provided the perovskite structure of the smaller strain (tolerance factor of 1.007). The conductivity of $(La_{0.8}Sr_{0.2})(Al_{0.9}Mg_{0.1})O_{2.85}$ with 72% relative density was higher than that of dense 8 mol% YSZ electrolyte.

## Appendix A. Size of oxygen vacancy

The size of oxygen vacancy in rare earth-doped ceria and rare earth-stabilized zirconia was calculated to be 0.1164 and 0.0993 nm, respectively, by Hong and Virkar [6]. The lattice parameter, $a_C$, of cubic perovskite ($ABO_3$) is related to the radii of A site cation ($r_A$), B site cation ($r_B$) and oxide ion ($r_O$) by Eqs. (A1) and (A2):

$$\text{A site} \quad \sqrt{2}a_C = 2r_A + 2r_O \quad (A1)$$

$$\text{B site} \quad a_C = 2r_B + 2r_O \quad (A2)$$

The prepared $(La_{1-x}Sr_x)(Al_{1-y}Mg_y)O_{3-\delta}$ perovskite solid solutions (LSAM) were identified as rhombohedral structure. The lattice parameter of rhombohedral, $a_R$, is equal to $\sqrt{2}a_C$. The effective radii of cation and anion are determined by Eqs. (A3)–(A5) for LSAM:

$$r_A = (1-x)r_{La} + x r_{Sr} \quad (A3)$$

$$r_B = (1-y)r_{Al} + y r_{Mg} \quad (A4)$$

$$r_O = \frac{(3-0.5(x+y))}{3} r_O + \frac{0.5(x+y)}{3} r_{VO} \quad (A5)$$

Therefore the lattice parameter of perovskite LSAM is expressed by Eqs. (A6) and (A7) for A site substitution and B site substitution, respectively.

A site substitution

$$\sqrt{2}a_C = 2\left[(1-x)r_{La} + x r_{Sr}\right] + 2\left[\left\{1 - \frac{1}{6}(x+y)\right\} r_O + \frac{1}{6}(x+y) r_{VO}\right] \quad (A6)$$

B site substitution

$$a_C = 2\left[(1-y)r_{Al} + y r_{Mg}\right] + 2\left[\left\{1 - \frac{1}{6}(x+y)\right\} r_O + \frac{1}{6}(x+y) r_{VO}\right] \quad (A7)$$

The lattice parameter $\sqrt{2}a_C$ of $LaAlO_3$ ($x = y = 0$) was calculated by Eqs. (A6) and (A7) using ionic radii of $La^{3+}$ (0.144 nm, coordination number 12), $Al^{3+}$ (0.0535 nm, coordination number 6) and $O^{2-}$ (0.140 nm, coordination number 6) to be 0.5520 nm for A site and 0.5473 nm for B site. The following multiplication factor, $f$, was introduced to explain the measured lattice parameter of $LaAlO_3$, $a_R = 0.5357$ nm of ICDD card, No. 85-1071:

$$\text{A-site} \quad f_A = \frac{0.5357}{0.5520} = 0.97047 \quad (A8)$$

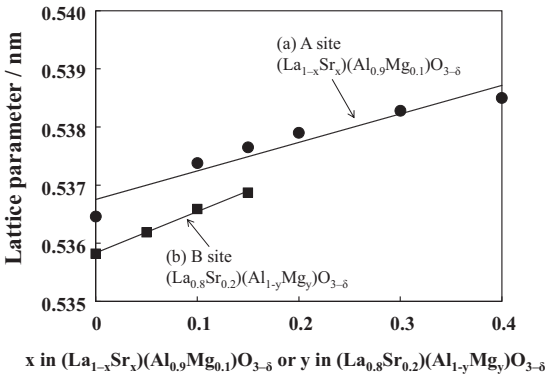


**Fig. A1.** Straight lines by the least squares method for the lattice parameters of $(La_{1-x}Sr_x)(Al_{0.9}Mg_{0.1})O_{3-\delta}$ and $(La_{0.8}Sr_{0.2})(Al_{1-y}Mg_y)O_{3-\delta}$ as functions of $x$ and $y$ values.

$$\text{B-site} \quad f_B = \frac{0.5357}{0.5473} = 0.97088 \tag{A9}$$

Fig. A1 shows the relationship between the measured lattice parameter and $x$ in $(La_{1-x}Sr_x)(Al_{0.9}Mg_{0.1})O_{3-\delta}$ or $y$ in $(La_{0.8}Sr_{0.2})(Al_{1-y}Mg_y)O_{3-\delta}$. The slope and intercept of line (a) correspond to $f_A$ $(-2r_{La} + 2r_{Sr} - r_O/3 + r_{VO}/3)$ and $f_A$ $(2r_{La} + 2r_O - yr_O/3 + yr_{VO}/3)$, respectively. The ionic radius of oxygen vacancy was calculated to be 0.1072 and 0.1729 nm from the slope and intercept of line (a). A similar relation was applied to line (b). The ionic radius of oxygen vacancy was calculated to be 0.0443 and 0.1415 nm from the slope and intercept, respectively. The size of oxygen vacancy in Ref. [6] was determined from the slope of the approximated straight lines. The above calculation suggests that the size of oxygen vacancy with A site substitution is different from that with B site substitution. A site substitution provides the larger oxygen vacancy (0.1072 nm) which is close to the size of oxygen vacancy (0.1164 nm) for doped ceria system in Ref. [6]. A more careful treatment may be needed to interpret the size of oxygen vacancy.

## References

[1] T. Ishihara, H. Matsuda and Y. Takita, J. Am. Chem. Soc., 116, 3801–3803 (1994).
[2] K. Shiratani, Y. Hirata, S. Sameshima, N. Matsunaga and S. Nakahara, Ceram. Int., 37, 1525–1531 (2011).
[3] D. Moriyama, Y. Hirata, S. Sameshima, N. Matsunaga, T. Doi, N. Kashima and S. Nagaya, J. Ceram. Soc. Jpn., 117, 635–638 (2009).
[4] S. Sameshima, D. Moriyama, Y. Hirata and N. Matsunaga, Mater. Chem. Phys., 125, 191–195 (2011).
[5] R.D. Shannon, Acta Cryst., A32, 751–767 (1976).
[6] S.J. Hong and A.V. Virkar, J. Am. Ceram. Soc., 78, 433–439 (1995).
[7] T.L. Nguyen, M. Dokiya, S. Wang, H. Tagawa and T. Hashimoto, Solid State Ionics, 130, 229–241 (2000).
[8] C.B. Choundhary, H.S. Maiti and E.C. Subbarao, in Solid Electrolytes and Their Applications, Ed. by E.C. Subbarao, Plenum Press, New York (1980) p. 40.
[9] S. Sameshima, H. Ono, K. Higashi, K. Sonoda, Y. Hirata and Y. Ikuma, J. Ceram. Soc. Jpn., 108, 1060–1066 (2000).
[10] T.Y. Chen, R.Y. Pan and K.Z. Fung, J. Phys. Chem. Solids, 69, 540–546 (2008).
[11] E.M. Levin, C.R. Robbins and H.F. WcMurdie, in Phase Diagrams for Ceramists, Ed. by M.K. Reser, The American Ceramic Society, Ohio (1964) p. 122, Fig. 312 (work of Schneider et al.).
[12] H. Inaba, H. Hayashi and M. Suzuki, Solid State Ionics, 144, 99–108 (2001).
[13] A. Hara, Y. Hirata, S. Sameshima, N. Matsunaga and T. Horita, J. Ceram. Soc. Jpn., 116, 291–297 (2008).
[14] J.Y. Park and G.M. Choi, Solid State Ionics, 154–155, 535–540 (2002).
[15] G. Qin, X. Huang, J. Chen and Z. He, Powder Technol., 235, 880–885 (2013).